Supplementary Information (SI) for Journal of Materials Chemistry A.

Supplementary Information for

Deciphering Carrier Thermodynamics and Kinetics Manipulation in Molecular Engineering of Graphitic Carbon Nitrides for Improved Visible-Light-Driven CO_2 Reduction

Ying Zhang[a]*, Jingxing Li[a,b]

[a] MIIT Key Laboratory of Thermal Control of Electronic Equipment, School of Energy and Power Engineering, Nanjing University of Science and Technology, Nanjing, 210094, China.

[b] Department of Chemical Engineering, Imperial College London, London, SW7 2AZ, UK.

1 Experimental detail

1.1 Chemicals

Urea, acetonitrile (ACN), and triethanolamine (TEOA) were purchased from Aladdin. Cobalt chloride ($CoCl_2{\cdot}6H_2O$) and all the bpy precursors (including bpy, dmbpy, dOMebpy, and dabpy) were purchased from Mecklin.

1.2 Characterization methods

The morphology and structure of these CN photocatalysts were characterized by transmission electron microscopy (TEM, JEOL2100F, JEOL), X-ray diffraction spectroscopy (XRD, D8 Advance, Bruker), The 13C cross-polarization magical angle spinning solid state NMR analysis (AVANCE III WB 400MHz, Bruker), UV–vis diffuse reflectance spectroscopy (UV-3600i Plus, Shimadzu), and Fourier transform infrared spectrometry (FTIR, Nicolet iS50, Thermo Fisher). A photoluminescence spectrometer (FLS 1000, Edinburgh Instruments) was employed for the steady-state and time-resolved photoluminescence (PL and TRPL) spectroscopic measurements. The transient absorption spectroscopy (TAS) was measured with a femtosecond pulsed laser (Pharos-Orpheus, Light Conversion, laser pulse width <190 fs, and the pulse frequency was set to 50 kHz,) and a transient absorption spectrometer (TA100, Time-Tech Spectra), exhibiting a temporal resolution of ~0.4 ps. The pump laser wavelength was set to 375 or 450 nm, and two continuum white-light probe windows with spectral ranges of 400−675 and 1050−1700 nm were measured separately. These spectroscopies were repeated at least 2–3 times, so averaged spectra can be obtained with an error of less than 10%. The electrochemical Mott-Schottky experiments were conducted with an electrochemical workstation (CHI 660C, Shanghai Chenhua). A sample-coated glassy carbon electrode was utilized as the working electrode, a platinum plate as the counter electrode, and an Ag/AgCl wire electrode as the reference electrode. The impedance (IMPE) curves were collected in a phosphate buffer solution (pH 6.65, consisting of 0.3 mol L^{-1} K_2SO_4, 0.1 mol L^{-1} KH_2PO_4, and 0.1 mol L^{-1} K_2HPO_4).

1.3 Additional photocatalytic CO_2 reduction evaluation

The $^{13}CO_2$ isotope-labeling experiment was performed using isotopic $^{13}CO_2$ (>99%) as reactant gas, diluted by Ar. The yielded products were analyzed by gas chromatography-mass spectrometry (GC-MS, Shimadzu QP2020 NX) equipped with an HP-PLOT/Q column. In the total ion chromatography (TIC), the peaks at retention time of 2.0 and 2.8 min correspond to the CO product and feed gas CO_2, respectively.

The apparent quantum yield (AQY) evaluation was performed with a top-irradiation quartz reactor which has a diameter of 1 cm. A 420 nm bandpass filter was equipped on the Xe-lamp to generate single wavelength irradiation. The 420-nm photon flux was controlled at 100~200 mW cm^{-2}, and the photocatalysis irradiation lasted 600 s. The following equation was applied, AQY(CO) = (amount of generated CO × 2) / (amount of incident photons) × 100%.

2 Supplementary data

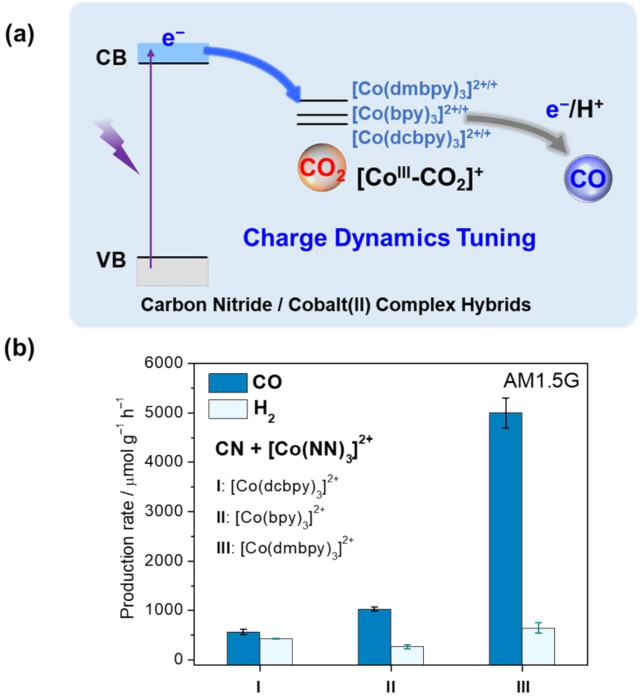

Figure S1. (a) Charge-transfer characteristics for the CN/$[Co(NN)_3]^{2+}$ hybrid photocatalytic CO_2 reduction system, (b) the photocatalytic CO_2 reduction performance over various cobalt(II) complexes (NN = diimine ligand, e.g., dcbpy = 2,2’-bipyridine-4,4’-dicarboxylic acid, bpy = 2,2’-bipyridine, dmbpy = 4,4’-dimethyl-2,2’-bipyridine). The reaction condition is, 5 mg CN, 1 μmol $[Co(NN)_3]^{2+}$, excessive ligands, and 20 μL ultrapure water as proton source were dispersed in a 6 mL CO_2-saturated ACN/TEOA (5:1 v:v) solution, irradiated for 1 h by a Xe-lamp (equipped with an AM1.5G filter, center power adjusted to 200 mW cm^{-2}).

Table S1. The elemental contents of the CN photocatalysts, measured by the elemental analysis*.

Catalysts	**N(wt%)**	**C(wt%)**	**H(wt%)**	**C/N (mol%)**
CN	60.77	34.91	1.56	0.670
CN-dOMe6	61.36	35.55	1.38	0.676
CN-da6	60.55	35.15	1.51	0.677
bpy	18.87	76.60	5.07	/

*The elemental analysis result in Table S1 suggests the overall elemental ratio was not obviously changed by the modification of the terminal groups, since the added amounts of the bpy moieties are quite light (only a few mg). The subtle increase in the C/N ratio (ca 1%) is reasonable when taking into account bpy-groups' participation in CN-dOMe6 and CN-da6.

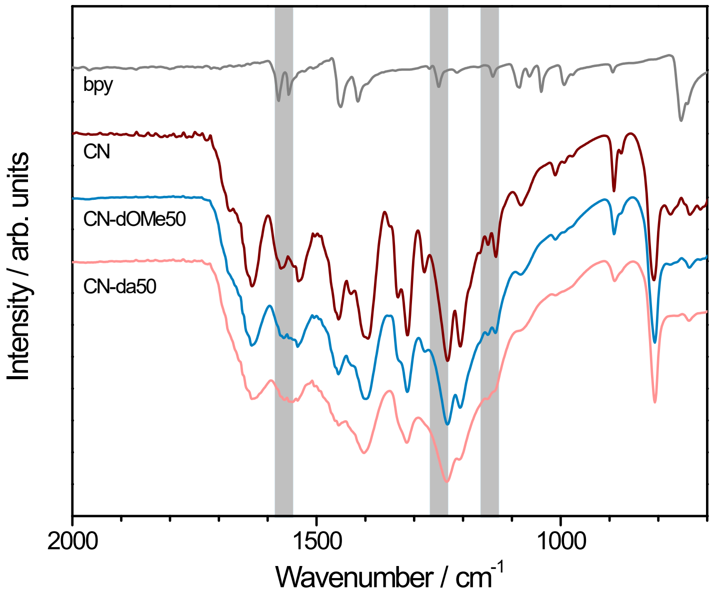

Figure S2. The FTIR vibration features of CN-dOMe50 and CN-da50 with terminal modification at a high loading weight. The emerging FTIR band at 1560 cm^{-1} as well as shoulders at 1250 and 1140 cm^{-1} are characteristic vibration features of the bipyridine rings.

Table S2. Fitting results of the ^{13}C CP-MAS NMR spectra.

Catalysts	**Peak* (ppm)**	**FWHM (ppm)**	**Area ratio (%)**	**$(CN_2NH+CN_2NH_2)/CN_3$**
CN	156.8	3.7	32.7	2.1
	162.9	2.7	15.6	
	165.3	3.3	51.6	
CN-dOMe6	156.9	3.7	32.0	2.1
	163.0	2.7	14.9	
	165.4	3.3	53.0	
CN-da2	156.9	3.9	34.0	1.9
	163.4	3.1	20.3	
	165.5	3.4	45.7	

*Low-field shifts of the $CN_2(NH_2)$ and $CN_2(NH)$ positions were observed for CN-dOMe6 and CN-da2, owing to the strong electron-withdrawing effect of pyridine rings compared with the heptazine heterocycles.

Table S3. XPS peak fitting results.

	C 1s			
	N─C=N **(288.1 eV)**	**C─O/C─N** **(286.5 eV)**	**C─C/C=C** **(284.8 eV)**	
CN	93.3%	2.1%	4.5%	
CN-dOMe6	92.9%	2.5%	4.6%	
CN-dOMe10	80.3%	3.8%	15.9%	
CN-da2	91.8%	1.1%	6.9%	
CN-da6	86.6%	1.5%	11.9%	
	N 1s			
	C=N─C	**N─C$_3$** **(400.0 eV)**	**C─NH$_x$** **(401.2 eV)**	**C=N─C/N─R$_3$***
CN	72.5% **(398.6 eV)**	22.5%	5.0%	2.64
CN-dOMe6	70.6% **(398.6 eV)**	24.9%	4.5%	2.40
CN-dOMe10	67.8% **(398.6 eV)**	25.9%	6.2%	2.11
CN-da2	69.9% **(398.7 eV)**	24.7%	5.4%	2.32
CN-da6	69.6% **(398.7 eV)**	25.7%	4.6%	2.30

*In N1s XPS fittings, the N─C$_3$ feature at 400.0 eV within the CN-dOMe*x* series increases to 24.9%~25.9%, and accordingly, the C═N─C peak component decreases to 70.6% and lower; for the CN-da*x* series, a higher N─C$_3$ contribution (24.7%~25.7%) was observed. The N sp^2/N sp^3 area ratio declines from 2.64 to 2.11. These hints suggest the bpy moieties anchor onto the heptazine and form new tricoordinated N─R$_3$ (R = C or H) sites.

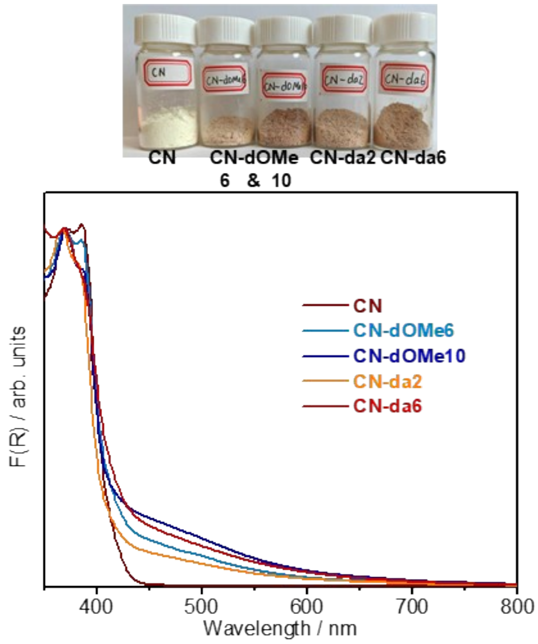

Figure S3. UV–vis diffuse reflectance spectra of the CN series; the inset is a photograph of these photocatalyst powders.

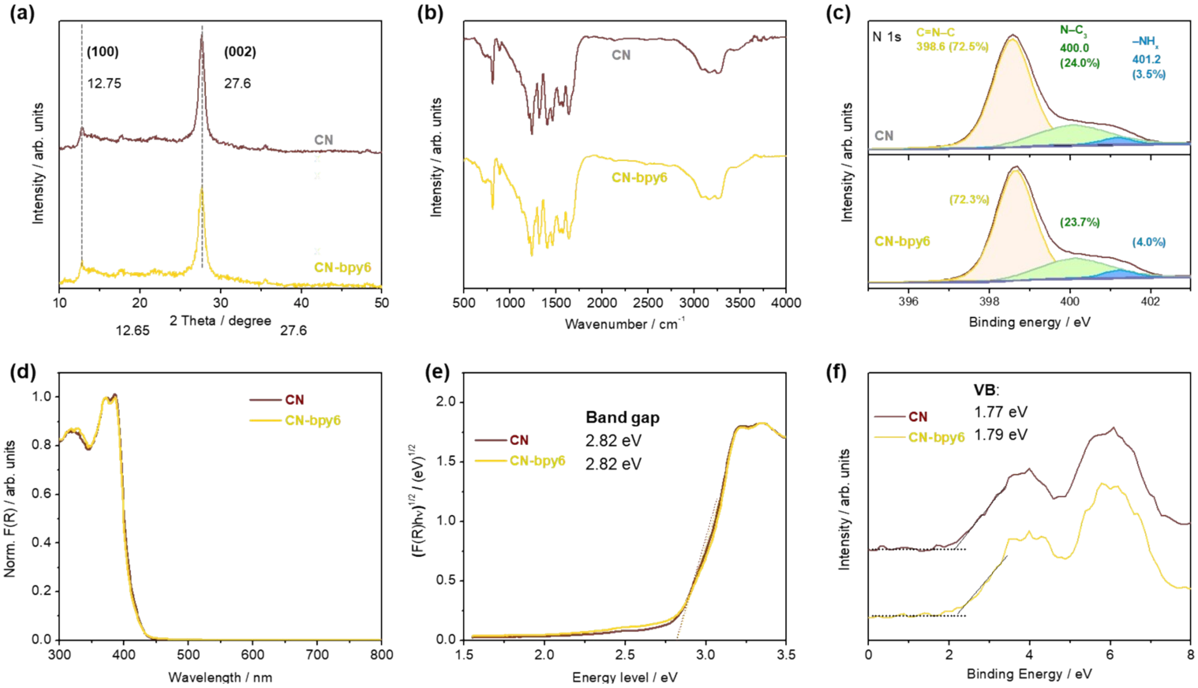

Figure S4. A comparison between CN and CN-bpy6 in their (a) XRD patterns, (b) FTIR spectra, (c) XPS N 1s spectra, (d) UV–vis diffuse reflectance spectra, (e) Tauc plots, (f) valence band XPS. One of the prerequisites for a successful thermal copolymerization is the anchoring groups on the bipyridine rings. When comparing the chemical and electronic structures between CN and CN-bpy6, all these structural features display the same, suggesting CN-bpy6 is a fake name, but exactly the same as the pristine CN. This is because the bpy precursor tends to totally decompose before urea's thermal polymerization, thus it does not influence the copolymerization process of urea to CN.

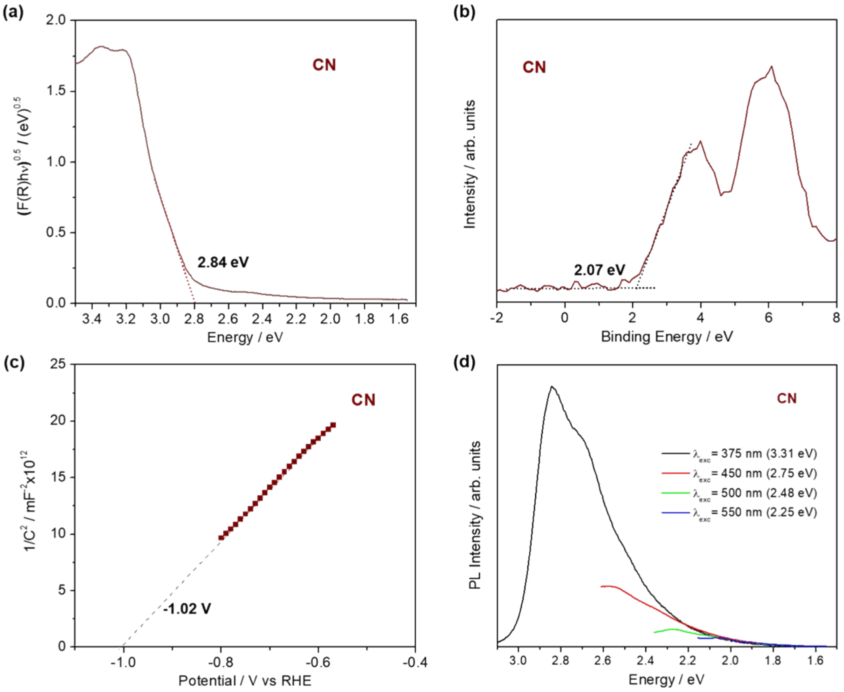

Figure S5. The energy band structure of CN addressed by spectroscopies and electrochemical measurements. (a) Tauc plot derived from UV–vis absorption spectrum, (b) valence band XPS, (c) Mott-Schottky plot, (d) PL spectra.

For pristine CN, the band gap energy of 2.84 eV was calculated by the Tauc plot derived from the UV–vis absorption spectrum, referring to the π-π* transitions of the heptazine ring. From our previously calculated molecular orbitals and literature, the highest occupied molecular orbitals (HOMOs) are located at the N atoms, and the lowest unoccupied molecular orbital (LUMO) consists of hybridized C and N atoms, forming respective π and π* orbitals.[1,2] Whereas the forbidden n–π* transitions of the conjugated heptazine units (~2.5 eV, associated with those mid-gap states), are quite weak. This agrees with the coplanar conjugation structure of the pristine CN.[3]

The binding energy in the valence band XPS was derived to be 2.07 eV; taking into account the XPS instrument's work function (4.2 eV) and the vacuum energy conversion ($E_{\text{vs vac}} = -E_{\text{vs NHE, pH = 0}} - 4.5$ eV), E_{VB} was determined to be 1.77 V vs NHE (pH = 0). Accordingly, the E_{CB} value appears to be −1.07 V vs NHE (pH = 0). With respect to the Mott-Schottky plot, the positive slope suggests its n-type feature, and the flat band potential was determined to be −1.02 V vs RHE, in accordance with the results derived from the valence band spectrum in XPS.

In particular, PL spectra with various excitation wavelengths were recorded for the CN either as powder or colloid (in Figures S5d and S6). The uniform emission profiles upon excitation at 340–440 nm indicate these PL features come from the same emitting states.

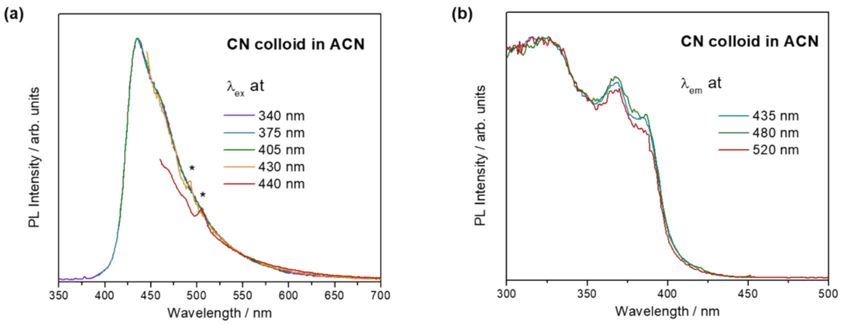

Figure S6. PL spectra of ultrasonically exfoliated CN colloid, 0.1 mg mL^{-1} in ACN, (a) normalized emission spectra upon various excitation wavelengths, and (b) excitation spectra collected at various emission wavelengths. *marks the Raman peak of solvent ACN. The uniform profiles upon 340–440 nm excitation indicate these PL features come from the same emitting states.

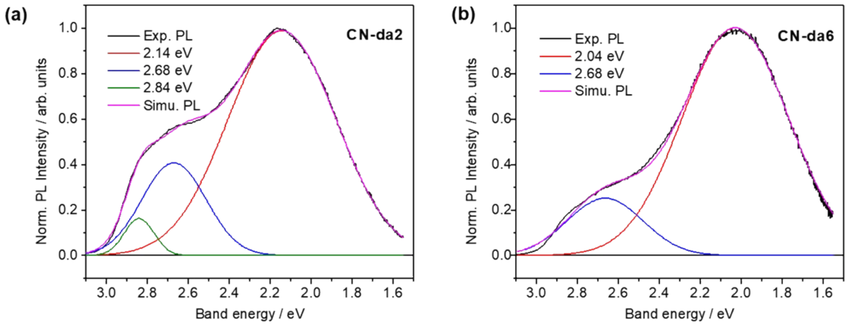

Figure S7. Gaussian simulation of PL spectra upon excitation at 375 nm, for (a) CN-da2 and (b) CN-da6. The center energies of the individual PL bands are indicated in the legends, and the cumulative simulation spectra show a good agreement with the experimental data.

Table S4. Fitting results of TRPL decays for the CN photocatalysts, excited at 375 nm*.

Sample	$\mathbf{a_1}$	$\boldsymbol{\tau_1}$ **/ ns**	$\mathbf{a_2}$	$\boldsymbol{\tau_2}$ **/ ns**	$\boldsymbol{\tau_{av}}$ **/ ns**
Collected at 460 nm					
CN	0.79±0.01	1.25±0.02	0.21±0.01	7.6±0.1	2.58±0.05
CN-dOMe6	0.87±0.01	0.82±0.02	0.13±0.01	4.8±0.1	1.34±0.05
CN-dOMe10	0.89±0.01	0.45±0.02	0.11±0.01	2.9±0.1	0.72±0.05
CN-da2	0.87±0.01	0.77±0.02	0.13±0.01	5.1±0.1	1.33±0.05
CN-da6	0.90±0.01	0.35±0.02	0.10±0.01	2.9±0.1	0.61±0.05
Collected at 600 nm					
CN	0.74±0.01	1.55±0.1	0.26±0.01	9.4±0.2	3.60±0.2
CN-dOMe6	0.74±0.01	1.72±0.01	0.26±0.01	6.2±0.1	2.88±0.02
CN-dOMe10	0.80±0.01	0.88±0.01	0.20±0.01	4.0±0.1	1.48±0.02
CN-da2	0.76±0.01	1.48±0.02	0.24±0.01	5.9±0.1	2.55±0.05
CN-da6	0.84±0.01	0.58±0.02	0.16±0.01	3.5±0.1	1.14±0.05

*A two-component exponential function was utilized, as the IRF curve deconvolved (FWHM of ca 0.13 ns):

$$I(t) = a_1 * exp\left(-\frac{t}{\tau_1}\right) + a_2 * exp\left(-\frac{t}{\tau_2}\right)$$

$$\tau av = \sum_j aj\tau j$$

The two emission components come from excitons of different localized spatial distances.[4]

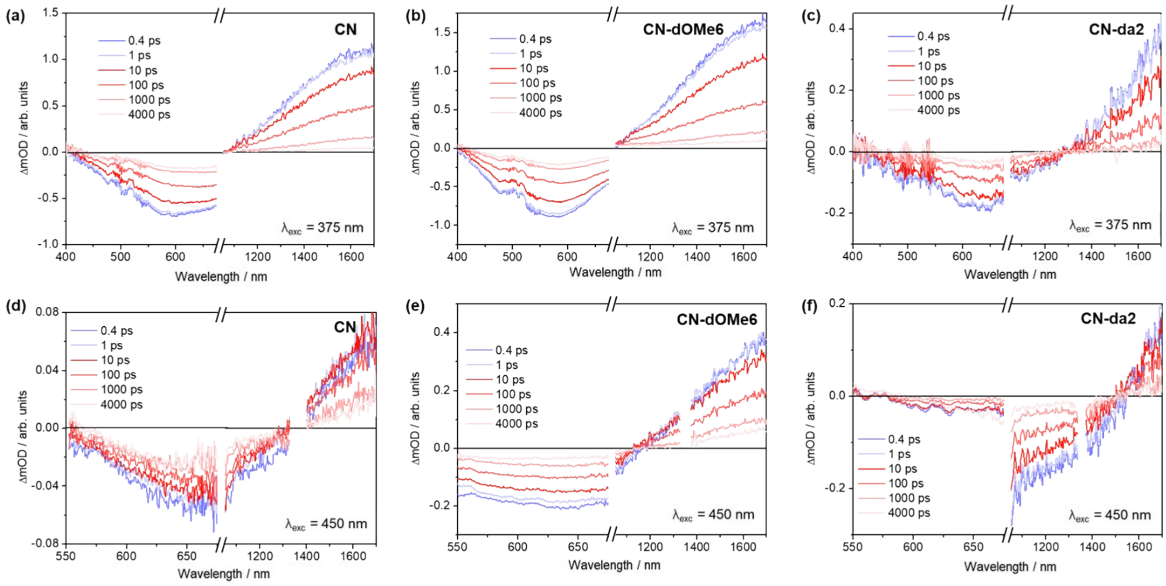

Figure S8. (a–c) Ultrafast fs-TA spectra at increasing delay times for (a,d) CN, (b,e) CN-dOMe6, and (c,f) CN-da2. The pump laser was (a–c) 375 nm and (d–f) 450 nm, with a pump pulse fluence of 80 nJ.

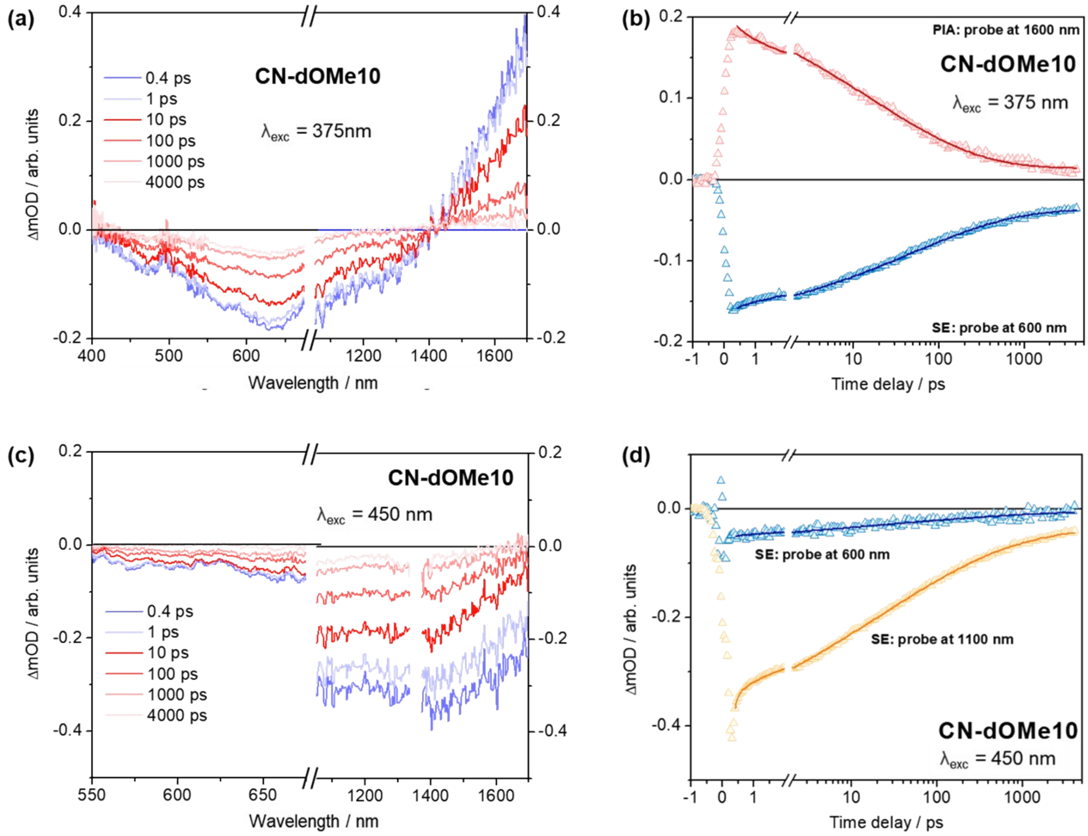

Figure S9. (a) Fs-TA spectra at increasing delay times for CN-dOMe10 at a pump wavelength of (a) 375 nm and (c) 450 nm, (b) TA decay kinetics at probing wavelengths of 600 and 1600 nm upon 375 nm excitation. (d) TA decay kinetics at probing wavelengths of 600 and 1100 nm, the same decay lifetime was observed.

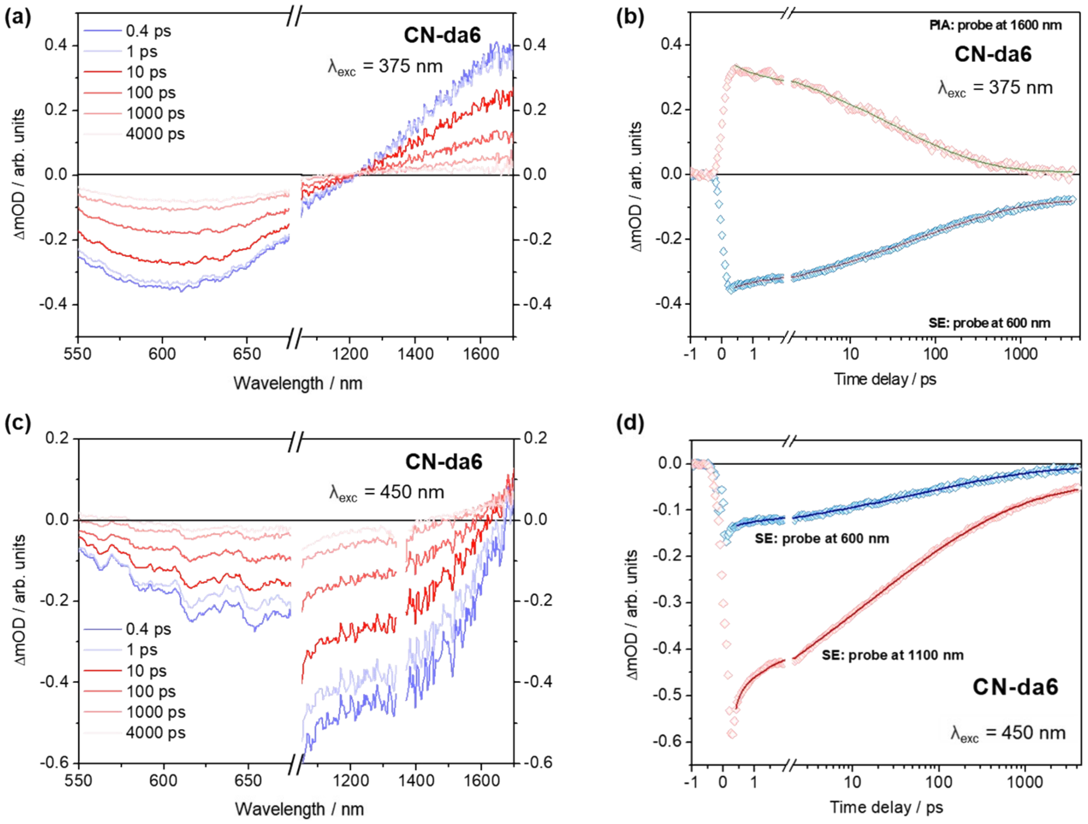

Figure S10. (a) Fs-TA spectra at increasing delay times for CN-da6 at a pump wavelength of (a) 375 nm and (c) 450 nm, (b) TA decay kinetics at probing wavelengths of 600 and 1600 nm upon 375 nm excitation. (d) TA decay kinetics at probing wavelengths of 600 and 1100 nm, the same decay lifetime was observed.

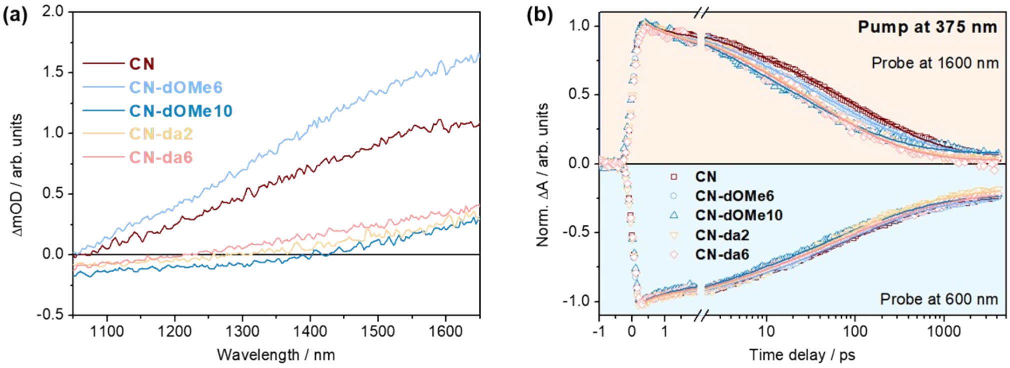

Figure S11. (a) A collection of TA spectra recorded at a delay time of 0.4 ps, upon excitation at 375 nm. (b) Normalized fs-TA decay kinetics at probing wavelengths of 1600 (upper panel) and 600 nm (lower panel); the scatters represent the experimental data and the solid lines are fitting results.

Note S1:

Upon 375 nm UV-light irradiation, all these photocatalysts exhibit positive PIA signal in the NIR region (as shown in Figure S11a). Amongst, CN and CN-dOMe6 have the stronger PIA intensities beyond the others, suggesting a high concentration of electrons within edges and STSs. In addition, the kinetics of the shallow-trapped electron were analyzed, and the 1600 nm-PIA decay curves were plotted as a function of time delay in Figure S11b. As the PIA signal involves electron trapping-detrapping, a stretched exponential decay function (1) was utilized to fit the decay curves.

$$\Delta A(t) = a_1 exp\left[-\left(\frac{t}{\tau_1}\right)^{\beta}\right] + inf \qquad \text{(S1)}$$

$$< \tau_1 > = \tau_1 \Gamma(\beta^{-1})/\beta \qquad \text{(S2)}$$

The parameter τ_1 in Equation S1 reflects a characteristic time constant for the electrons in the shallow-trap states, and β reflects the heterogeneity; the averaged lifetime $<\tau_1>$ was calculated by using the gamma function in Equation S2. The "inf" (infinite) component indicates the ultralong-lived process with regard to the temporal window, referring to a small contribution from the deep-trap states.

A perfect agreement can be observed between the experimental scatters and the fitted solid lines, and the fitting parameters obtained are summarized in Table S5. The large amplitude a_1 to "inf" ratios (~0.9:0.1) confirm that the shallow-trapped electrons dominate these CN photocatalysts.[5] Looking into the details, the averaged lifetimes $<\tau_1>$ of the modified CN photocatalysts (63~136 ps) are relatively shorter than that of the pristine CN (176 ps), pointing out a kinetic side-effect of the activated mid-gap states upon UV light irradiation.

In general, the SE decay shows comparable kinetics for all the CN photocatalysts, as evidenced by the fitting results in Table S5. The SE characteristics display a similar time constant τ_1 of ca. 100 ps, which is a majority contribution from the shallow-trapped electrons, as well as a residual long-lived emitting component associated with those relatively lower lying STSs.

Table S5. The TAS decay kinetics for the CN photocatalysts excited at 375 nm and fitted using a combined stretched-exponential decay function.*

Sample	Pump/Probe (nm)	a_1	τ_1 (ps)	β	inf	$<\tau_1>$ (ps)
CN	375/600	0.73	67±5	0.44±0.02	0.27	175±25
	375/1600	0.90	72±8	0.45±0.01	0.10	179±25
CN-dOMe6	375/600	0.72	62±4	0.45±0.01	0.28	154±20
	375/1600	0.91	45±4	0.41±0.02	0.09	140±20
CN-dOMe10	375/600	0.75	43±6	0.42±0.02	0.25	126±15
	375/1600	0.91	18±1	0.39±0.02	0.09	64±10
CN-da2	375/600	0.77	56±5	0.44±0.01	0.23	146±22
	375/1600	0.94	31±1	0.44±0.02	0.06	81±11
CN-da6	375/600	0.76	55±5	0.39±0.01	0.24	196±35
	375/1600	0.95	31±2	0.44±0.02	0.05	81±10

*The "inf" (infinite) component indicates an ultralong-lived process with regard to the temporal window.

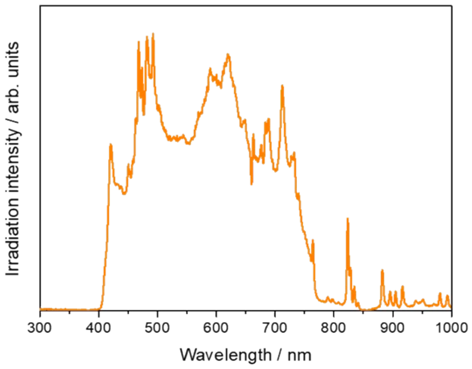

Figure S12. The irradiation spectrum of the Xe lamp used in this work, equipped with an AM1.5G filter and a 420 longpass cut filter.

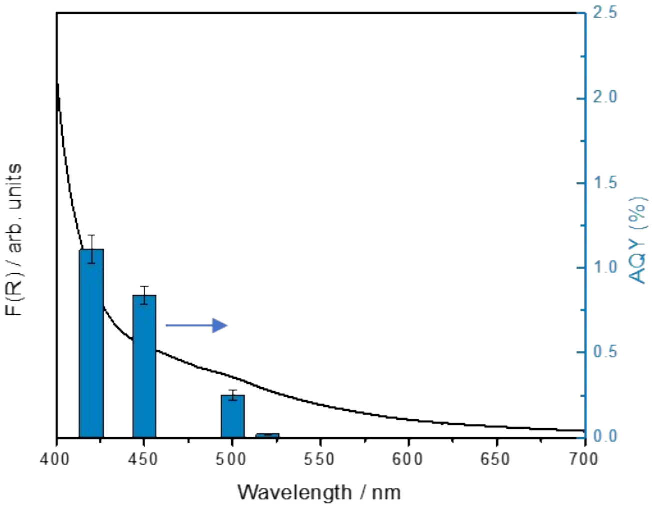

Figure S13. Apparent quantum yield (AQY) under single-wavelength irradiation for CN-OMe6 with its UV–vis diffuse reflectance spectrum for reference.

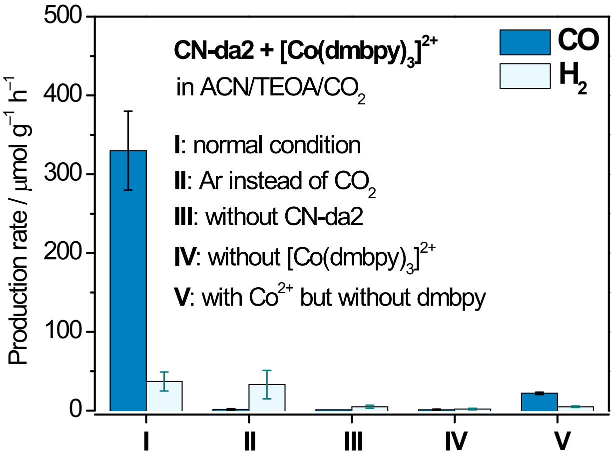

Figure S14. Production of CO and H_2 from the photocatalytic CO_2 reduction system under various reaction conditions for CN-da2 systems. The discussion is detailed in Note S2.

Note S2:

A series of control experiments was performed to elucidate the catalytic reaction, and the CO_2 gas is confirmed to be the only carbon source. For the control experiments in Figure S14, the initial reaction condition **I** is, 5 mg photocatalyst, 1 µmol $[Co(dmbpy)_3]^{2+}$, excessive dmbpy ligands, and 20 µL ultrapure water as proton source were dispersed in a 6 mL CO_2-saturated ACN/TEOA (5:1 v:v) solution, irradiated for 1 h by a Xe-lamp equipped with an AM1.5G filter and a 420 longpass cut filter (irradiation spectrum is shown in Figure S12, the irradiation power was adjusted to 90 mW cm^{-2}). Condition **II** confirms that CO_2 is the only carbon source to produce CO. Condition **III** emphasizes the importance of the initial photoexcitation and charge injection for the CN segment to the $[Co(dmbpy)_3]^{2+}$ cocatalyst. In the absence of $[Co(dmbpy)_3]^{2+}$ (Condition **IV**) the photocatalysis activities are poor, signifying that the active sites for both specific CO_2 conversion and non-specific H_2 evolution are located at the cobalt complex.

Interestingly noted in Figures S14 and 8f, a simple mixing of CN-dOMe6 (or CN-da2) photocatalyst and Co^{2+} metal center enables the CO_2 reduction activity, that is not observed for the pristine CN. This suggests a coordination bondage between the Co^{2+} center ion and the terminal dOMebpy/dabpy within the CN-dOMe6 and CN-da2 photocatalysts, forming the active $[Co(diimine)_3]^{2+}$. The electron transfer from the excited CN to the cobalt(II) complexes also becomes feasible, which was proven by the PL dynamic quenching shown in Figure S18 and Table S6.

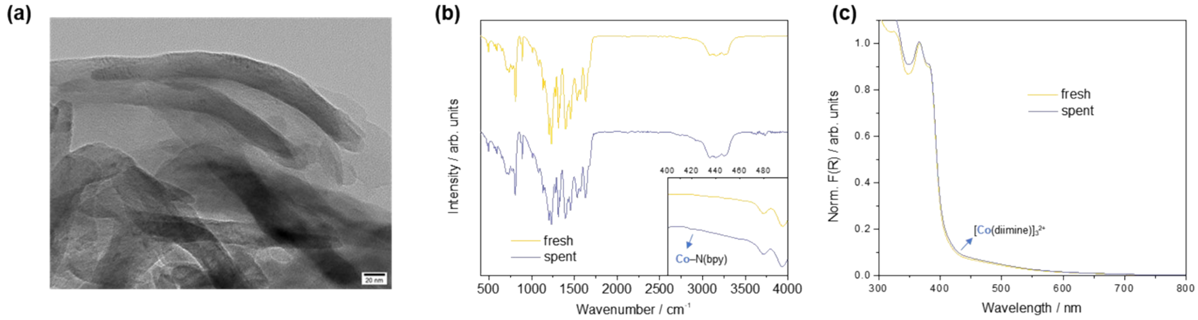

Figure S15. Characterization of the spent CN-dOMe6 photocatalyst, (a) HRTEM image, (b) FTIR spectra, and (c) UV–vis diffuse reflectance spectra. An enlarged FTIR spectral region of 400–500 cm^{-1} is shown in the (b) inset. Detailed analysis is discussed in Note S3.

Note S3:

Comprehensive characterizations were carried out for the spent CN-dOMe6 photocatalyst by using HRTEM, ICP-OES, FTIR, and UV–vis diffuse reflectance spectroscopy. The spent CN-dOMe6 powder was collected after photocatalytic CO_2 reduction, subjected to three cycles of centrifugation and washing, and then dried in the oven. The HRTEM image in Figure S15a confirms that the spent CN-dOMe6 powder retains its original thin sheet-like morphology. The post-reaction FTIR characterization (Figure S15b) shows that the characteristic vibrational IR bands of the heptazine heterocycles (at 809 and 1200–1700 cm^{-1}) and the terminal $–NH_x$ groups (at 891 and 3000–3400 cm^{-1}) are identical to those of the fresh sample, indicating the robustness of the CN framework structure. Furthermore, a small band emerges at 420 cm^{-1} for the spent CN-dOMe6 (inset of Figure S15b), attributed to the Co^{2+}–N(bpy) bonding. This suggests the successful formation of a linkage between the terminal bipyridine groups on the CN framework and the Co^{II} cocatalyst. This strong interaction between the Co^{II} metal center and the anchored terminal bipyridine groups, rather than merely physically adsorbed or dissolved $[Co(dmbpy)_3]^{2+}$, was confirmed by ICP-OES analysis. A residual Co loading of 0.1% was detected for the spent CN-dOMe6 powder even after three cycles of centrifugation and washing. Such chelation was also supported by its UV–vis diffuse reflectance spectrum (Figure S15c), which displays a slight increase in absorption around the typical 450 nm.

In conclusion, these results demonstrate that the morphology, structure, and composition of the CN-dOMe6 photocatalyst are highly stable throughout the photocatalytic process. Additionally, the formation of Co^{2+} chelation with the terminal bipyridine groups is observed, which should benefit electron transfer from the excited CN-dOMe6 to the active Co^{2+} cocatalyst sites.

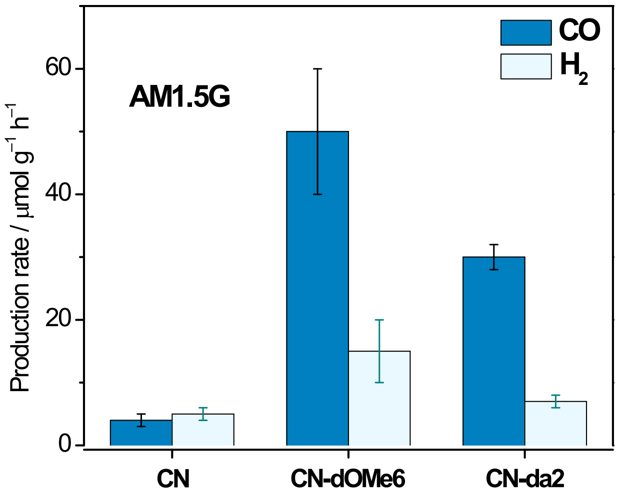

Figure S16. Photocatalytic CO_2 reduction performance of the CN photocatalysts with Co^{2+} as cocatalyst but without dmbpy ligand. The Xe-lamp is equipped with an AM1.5G filter and a 420 longpass cut filter to mimic the visible solar light spectrum. The reaction condition is, 5 mg photocatalyst in a mixture of ACN/TEOA (5:1 v:v) serves as solvent and electron sacrificial donor, 1 μmol Co^{2+} added but without dmbpy ligand.

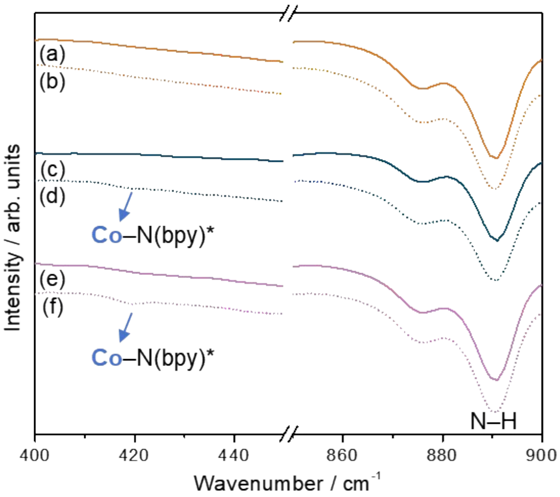

Figure S17. FTIR spectra the CN-based photocatalysts and after Co^{2+} loading: (a) CN, (c) CN-dOMe6, (e) CN-dOMe10, and the corresponding Co^{2+}-loaded composites (b) CN/Co^{2+}, (d) CN-dOMe6/Co^{2+}, (f) CN-dOMe10/Co^{2+}. These composites were prepared by stirring the CN series catalysts with $CoCl_2$ solution for 24 h, followed by centrifugation and washing for three times.

*Both the FTIR spectra of CN-dOMe6/Co^{2+} and CN-dOMe10/Co^{2+} composites exhibit a distinct new characteristic band at 420 cm^{-1} , which is absent in the pristine catalysts CN-dOMe6 and CN-dOMe10 as well as the mixture of CN and Co^{2+}. The 420 cm^{-1} band originates from the Co−N stretching vibration. Its appearance at this specific wavenumber is consistent with literature reports on strong Co^{2+}–N bonding in Co^{2+}–bipyridine bidentate chelation.[6,7] Conversely, the N−H vibration at 891 cm^{-1} (attributed to the terminal NH_x groups on CN framework) remains unchanged, indicating that the coordination occurs specifically at the bipyridine sites rather than the heptazine ring edges.

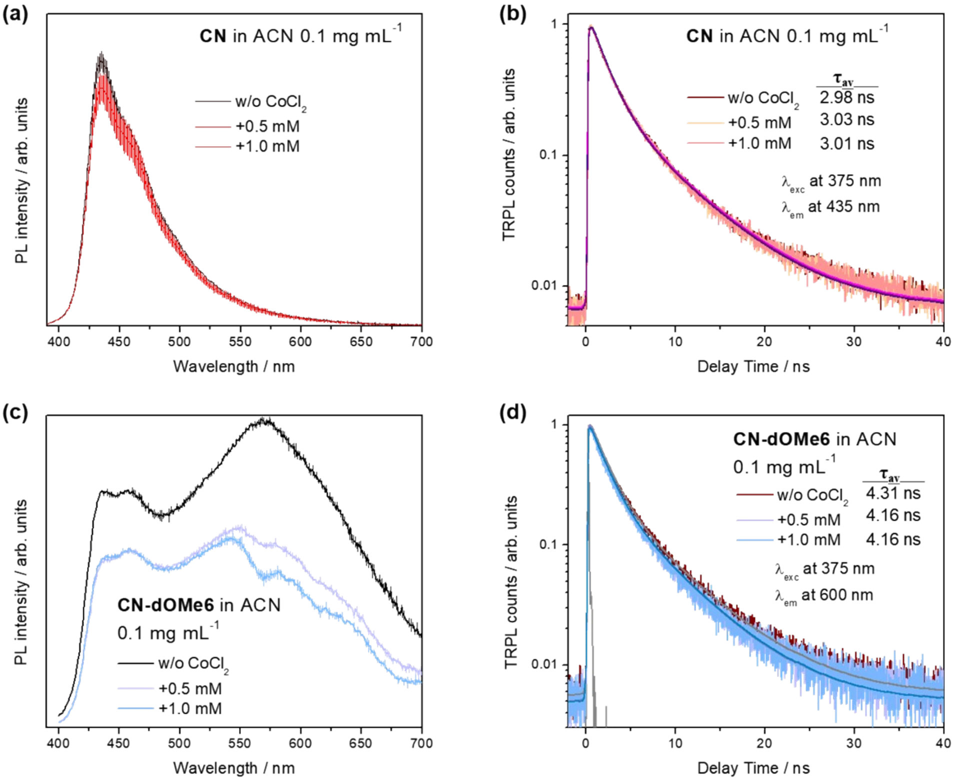

Figure S18. The steady-state PL spectra of (a) CN and (c) CN-dOMe6 in 0.1 mg mL^{-1} ACN suspension upon excitation at 375 nm, before and after adding 0.5 mM Co^{2+}. The TRPL decays of (b) CN and (d) CN-dOMe6. Neither of the steady-state PL or TRPL decays of the pristine CN was influenced by the addition of Co^{2+}, suggesting lacking of interaction between the CN fragment and the cocatalyst. In contrast, a pronounced PL quenching was observed for the CN-dOMe6 STS electrons in the region of 500–700 nm. The TRPL decays also accelerated, providing direct evidence for the advantageous electron transfer from the CN-dOMe6 to the Co^{2+} cocatalyst site.

Table S6. Fitting results of TRPL decays for the CN photocatalysts in ACN.

Sample	+ Co^{2+} / mM	a_1	τ_1 / ns	a_2	τ_2 / ns	τ_{av} / ns
CN	0	80%	1.95	20%	7.10	2.98
	0.5	79%	1.98	21%	7.00	3.03
	1.0	80%	2.00	20%	7.04	3.01
CN-dOMe6	0	32%	1.59	68%	5.59	4.31
	0.5	29%	1.46	71%	5.26	4.16
	1.0	29%	1.46	71	5.26	4.16

Table S7. Summary of visible-light-driven CO_2 reduction performance over CN photocatalysts.

Photocatalyst	Cocatalyst	Sacrificial agent	Light source	CO production	AQY	Ref
CN	$[Co(dmbpy)_3]^{2+}$	TEOA	Xe lamp, >420 nm, 90 mW/cm^2	2.9 μmol/g/h	/	This work
CN-dOMe6	$[Co(dmbpy)_3]^{2+}$	TEOA		1171 μmol/g/h	1.11%@420 nm	
CN-da2	$[Co(dmbpy)_3]^{2+}$	TEOA		330 μmol/g/h	0.65%@420 nm	
CN-BINA	$[Co(bpy)_3]^{2+}$	TEOA	Xe lamp, >420 nm	162 μmol/g/h	n.a.	[8]
CN-bpy-Co	$[Co(bpy)_3]^{2+}$	TEOA	5W LED, >420 nm	106 μmol/g/h	n.a.	[9]
CoPc-COP @CN	CoPc	TEOA	300 W Xe lamp, >350 nm	133.8μmol/g/h	n.a.	[10]
Rh$_1$–bpy/CN	Rh–bpy	TEOA	Xe lamp, >420 nm, 264 mW/cm^2	13.2 μmol/g/h	0.0003%@420 nm	[11]
CN-Coqpy	Coqpy	BIH	Xe lamp, >400 nm	8 μmol/g/h	0.25%@>400 nm	[12]
CN-CV	$[Co(bpy)_3]^{2+}$	TEOA	300 W Xe lamp, >420 nm	717 μmol/g/h	1.9% @420 nm	[13]
Co^{SA}@CN	Co^{2+} site	TEOA	Xe lamp, >420 nm, 200 mW/cm^2	528 μmol/g/h	0.4% @420 nm	[14]

Reference

1 Y. Chen, B. Wang, S. Lin, Y. Zhang and X. Wang, *J. Phys. Chem. C*, 2014, **118**, 29981–29989.

2 X. Zhang, X. Xie, H. Wang, J. Zhang, B. Pan and Y. Xie, *J. Am. Chem. Soc.*, 2013, **135**, 18–21.

3 Y. Zhang, M. Cao, H. Feng, D. Liu and Q. Li, *ACS Catal.*, 2023, **13**, 11376–11388.

4 J. Yu, Y. Wang, Y. Zhou, W. Fang, B. Liu and J. Xing, *Nano Lett.*, 2024, **24**, 4439–4446.

5 S. Song, X. Zou, Y. Kang, X. Ji, R. Lu and A. Yu, *J Phys Chem C*, 2023, **127**, 10617–10628.

6 Y. Che, D. Chen, B. Wang, M. Li, Y. Zhao, G. Zhu and H. Xing, *J. Am. Chem. Soc.*, 2026, **148**, 5764–5773.

7 Y. Sabeg, R. Benali-Cherif, W. Falek, R. Takouachet, L. Golea, M. Aygün and N. Benali-Cherif, *Polyhedron*, 2025, **271**, 117445.

8 Z. Pan, P. Niu, M. Liu, G. Zhang, Z. Zhu and X. Wang, *ChemSusChem*, 2020, **13**, 888–892.

9 J. Wei, X. Chen, C. Liu, Q. Zhou, S. Tian, K. F. Wang and M. Lu, *Nanoscale*, 2023, **15**, 5036–5043.

10 J. Rong, Q. Xu, J. Han, K. Ren, J. Zhang, X. Zhao, P. She, J. S. Qin and H. Rao, *Chem. Eng. J.*, 2025, **507**, 160814.

11 L. Li, Y. Mao, J. Zhao, Y. Zhang, H. Wu and Q. Gu, *J. Mater. Chem. A*, 2024, **12**, 15762–15771.

12 B. Ma, G. Chen, C. Fave, L. Chen, R. Kuriki, K. Maeda, O. Ishitani, T. C. Lau, J. Bonin and M. Robert, *J. Am. Chem. Soc.*, 2020, **142**, 6188–6195.

13 P. Yang, H. Zhuzhang, R. Wang, W. Lin and X. Wang, *Angew Chem Int Ed*, 2019, **58**, 1134–1137.

14 P. Huang, J. Huang, S. A. Pantovich, A. D. Carl, T. G. Fenton, C. A. Caputo, R. L. Grimm, A. I. Frenkel and G. Li, *J. Am. Chem. Soc.*, 2018, **140**, 16042–16047.